

draft of February 25, 2024

Diffusive Shock Acceleration Simulations of Radio Relics

Hyesung Kang¹, Dongsu Ryu^{2,4}, and T. W. Jones³

¹*Department of Earth Sciences, Pusan National University, Pusan 609-735, Korea:
kang@uju.es.pusan.ac.kr*

²*Department of Astronomy and Space Science, Chungnam National University, Daejeon
305-764, Korea: ryu@canopus.cnu.ac.kr*

³*School of Physics and Astronomy, University of Minnesota, Minneapolis, MN 55455,
USA: twj@msi.umn.edu*

ABSTRACT

Recent radio observations have identified a class of structures, so-called radio relics, in clusters of galaxies. The radio emission from these sources is interpreted as synchrotron radiation from GeV electrons gyrating in μ G-level magnetic fields. Radio relics, located mostly in the outskirts of clusters, seem to associate with shock waves, especially those developed during mergers. In fact, they seem to be good structures to identify and probe such shocks in intracluster media (ICMs), provided we understand the electron acceleration and re-acceleration at those shocks. In this paper, we describe time-dependent simulations for diffusive shock acceleration at weak shocks that are expected to be found in ICMs. Freshly injected as well as pre-existing populations of cosmic-ray (CR) electrons are considered, and energy losses via synchrotron and inverse Compton are included. We then compare the synchrotron flux and spectral distributions estimated from the simulations with those in two well-observed radio relics in CIZA J2242.8+5301 and ZwCl0008.8+5215. Considering that the CR electron injection is rather inefficient at weak shocks with Mach number $M \lesssim$ a few, the existence of radio relics could indicate the pre-existing population of low-energy CR electrons in ICMs. The implication of our results on the merger shock scenario of radio relics is discussed.

Subject headings: acceleration of particles — cosmic rays — galaxies: clusters: general — shock waves

⁴Corresponding Author

1. INTRODUCTION

The presence of energetic nonthermal particles, especially electrons, in clusters of galaxies has been inferred from observations of so-called “radio halos” and “radio relics” (see, e.g., Carilli & Taylor 2002; Govoni & Feretti 2004; Ferrari et al. 2008; Brüggen et al. 2011, for reviews). The radio emission from these sources is interpreted as synchrotron radiation of cosmic-ray (CR) electrons. The radio halos center roughly in cluster cores and have low surface brightness with steep radio spectrum and low polarization. Radio relics, on the contrary, are isolated structures, typically located in the cluster outskirts but within virial radii. They often exhibit sharp edges, and most of them show strong polarization. In fact, with occasional pairings found in the opposite side of clusters and elongated morphologies, radio relics are commonly thought to reveal shock waves in intracluster media (ICMs) produced during mergers (e.g., Enßlin et al. 1998; Roettiger, Burns & Stone 1999; Miniati et al. 2001). Unfortunately, relics are found mostly too far from cluster cores for their X-ray signatures to be easily detected. So only in a few cases, their association with ICM shocks have been established by X-ray observations (e.g., Finoguenov et al. 2010; Akamatsu & Kawahara 2011). More than 40 relics have been identified in radio observations so far (Nuza et al. 2012, and references therein). Based on the spatial distribution of shocks seen in cluster formation simulations, it is predicted that coming radio surveys will easily identify hundreds more (e.g., Skillman et al. 2011; Vazza et al. 2012; Nuza et al. 2012).

The observed synchrotron radiation is expected to come from CR electrons with Lorentz factors $\gamma_e \gtrsim 10^4$, spiraling in $\sim \mu\text{G}$ magnetic fields. The cooling time scale of such CR electrons due to synchrotron emission and inverse Compton (IC) scattering does not much exceed $\sim 10^8$ yrs (see equation (2)). Advection or diffusion over that time would typically be limited to $\lesssim 100$ kpc. So, the electrons have very likely been injected, accelerated or re-accelerated close to where they are seen in emission.

Shocks, believed to be associated to observed radio relics, are obvious candidates for the acceleration or re-acceleration of the CR electrons. Suprathermal particles are known to be produced as an inevitable consequence of the formation of collisionless shocks in tenuous plasmas (e.g., Garaté & Spitkovsky 2012). If postshock suprathermal particles have sufficient rigidity to recross the shock transition, they can be further accelerated to become CRs through so-called Diffusive Shock Acceleration (DSA) (Bell 1978; Drury 1983; Malkov & Drury 2001). Only a very small fraction of inflowing plasma particles are “injected” from the thermal pool into the CR population. Yet, in strong shocks, a sufficient number of CRs reach high energies, so that they extract a substantial fraction of the dissipated energy, allowing DSA to be efficient.

Shock waves are indeed common in the intergalactic space (e.g., Miniati et al. 2000;

Ryu et al. 2003). They are induced by the supersonic flow motions produced during the hierarchical formation of the large-scale structure (LSS) in the universe. Those shocks are, in fact, the dominant means to dissipate the gravitational energy which is released during the LSS formation. They broadly reflect the dynamics of baryonic matter in the LSS of the universe, and, indirectly, dark matter. Simulations suggest that while very strong shocks form in relatively cooler environments in filaments and outside cluster virial radii, shocks produced by mergers and flow motions in hotter ICMs are relatively weak with Mach number $M \lesssim$ a few (Ryu et al. 2003; Pfrommer et al. 2006; Kang et al. 2007; Skillman et al. 2008; Hoeft et al. 2008; Vazza et al. 2009; Brüggén et al. 2011).

At weak shocks, however, DSA should be inefficient. This is expected from the fact that the particle energy spectrum associated with DSA is steep when the density compression across a shock is small. Also the relative difference between the postshock thermal and flow speeds is greater in weaker shocks. Consequently, the injection from thermal to nonthermal particles should be inefficient at weak shocks (e.g., Kang et al. 2007). At shocks with $M \lesssim$ a few, much less than $\sim 10^{-3}$ of protons are thought to be injected into CRs and much less than ~ 1 % of the shock ram pressure be converted into the downstream pressure of CR protons (Kang & Ryu 2010). For reference, recent Fermi observations of γ -ray emission from galaxy clusters, searching for γ -ray by-products of $p - p$ collisions, limit the pressure due to CR protons to less than ~ 10 % of the gas thermal pressure there (Abdo et al. 2010; Donnert et al. 2010). IACT (Imaging Atmospheric Cherenkov Technique) observations of TeV γ -ray suggest even a lower limit of $\lesssim 1 - 2$ % in core regions of some clusters (Alakšić et al. 2012; Arlen et al. 2012).

Injection and acceleration of electrons are even more problematic at weak shocks. Relativistic electrons and protons of the same energy are accelerated the same in DSA, since they have the same rigidity. But nonrelativistic electrons of a given energy have substantially smaller rigidities than protons, making them much harder to be injected at shocks from the thermal pool. As a consequence, the number of electrons injected and accelerated to the CR population is likely to be significantly smaller than that of CR protons, and so is the pressure of CR electrons at weak shocks.

Hot ICMs, on the other hand, should have gone first through accretion shocks of high Mach numbers around clusters and filaments and then through weaker shocks inside those nonlinear structures (Ryu et al. 2003; Kang et al. 2007). Hence, it is expected that ICMs contain some CR populations produced through DSA at the structure formation shocks. In addition, in ICMs, nonthermal particles can be produced via turbulent re-acceleration (e.g., Brunetti & Lazarian 2007, 2011). Moreover, secondary CR electrons are also continuously generated through $p - p$ collisions of CR protons with thermal protons of ICMs

(e.g., Miniati et al. 2001; Pfrommer & Enßlin 2004). If radio relics form in media with such “pre-existing” CRs, the problem of inefficient injection at weak shocks can be alleviated.

In this paper, we study DSA of CR electrons at shocks expected to be found in ICMs, with and without pre-existing CR electrons. Since the shocks are mostly weak, the CR pressure is likely to be a small fraction of the thermal pressure (see Kang & Ryu 2011). So we apply DSA in the test-particle regime. In the time-asymptotic limit without radiative losses, the test-particle DSA theory predicts a steady-state distribution of power-law for downstream CR electrons, $f_{e,2}(p) \propto p^{-q}$ with $q = 3\sigma/(\sigma - 1)$, where σ is the density compression ratio across a shock, when no pre-existing CR is assumed (Drury 1983). If pre-existing CR electrons of a power-law distribution, $f_{e,1} \propto p^{-s}$, are assumed, the distribution of re-accelerated electrons approaches $f_{e,2}(p) \propto p^{-r}$ with $r = \min(q, s)$ at large momenta (Kang & Ryu 2011, and also see equation (9)). The power-law distributions of $f_{e,2}(p)$ translate into the synchrotron/IC spectra of $j_\nu \propto \nu^{-\alpha}$ with $\alpha = (q - 3)/2$ or $(r - 3)/2$ (e.g., Zirakashvili & Aharonian 2007; Blasi 2010; Kang 2011). These properties provide essential benchmarks for expected spectral properties

We perform “time-dependent”, DSA simulations of CR electrons for plane-parallel shocks, which include the energy losses due to synchrotron and IC processes. Using the simulation data, we calculate the synchrotron emission from CR electrons, and model the synchrotron flux and spectral distributions from spherical shocks. We then compare the resulting distributions to those of two well-observed radio relics in clusters CIZA J2242.8+5301 (van Weeren et al. 2010) and ZwCl0008.8+5215 (van Weeren et al. 2011) in details.

The relic in CIZA J2242.8+5301 at redshift $z = 0.1921$ perhaps demonstrates the best evidence for DSA at merger shocks. It is located at a distance of ~ 1.5 Mpc from the cluster center and spans ~ 2 Mpc in length. The relic shows a spectral index gradient towards the cluster center. The spectral index, measured between 2.3 and 0.61 GHz, steepens from -0.6 to -2.0 across the relic. The relic is strongly polarized at the 50 – 60 % level, indicating ordered magnetic fields aligned with the relic. In the opposite, southern part of the cluster, an accompanying fainter and smaller relic is found. The relic in ZwCl0008.8+5215 at $z = 0.1032$ is found at a distance of ~ 0.85 Mpc from the cluster center and has a linear extension of ~ 1.4 Mpc. It also shows the steepening of the spectral index towards the cluster center. The spectral index, measured between 1382 and 241 MHz, changes from -1.2 to -2.0 across the relic. The polarization fraction is less with $\lesssim 25$ %. It also has an accompanying relic of a linear extension of ~ 290 kpc in the opposite, western side of the cluster.

In Section 2 we describe the numerical method and the models for magnetic field, diffusion, electron injection, and pre-existing CR electron population. We present analytic evaluations for some features in the CR electron energy spectrum and synchrotron emission

spectrum in Section 3. The results of simulations are presented and compared with observations of the previously mentioned radio relics in Section 4. Summary follows in Section 5.

2. DSA SIMULATIONS OF CR ELECTRONS

2.1. Numerical Method

We simulate DSA of CR electrons at gasdynamical shocks in one-dimensional plane-parallel geometry. Shocks in ICs, especially merger shocks, are expected to persist over $\gtrsim 10^9$ yrs, a substantial fraction of the cluster lifetime (e.g., Skillman et al. 2011). On the other hand, the time scales over which electrons are accelerated and cool are much shorter (see Eq. [2] below). So we assume that the shock structure remains steady. Assuming that the CR feedback to the flow is negligible at weak shocks in the test-particle limit, the background flow, u , is given by the usual shock jump condition. Then, the time-dependent evolution of the CR electron distribution, $f_e(t, x, p)$, which is averaged over pitch angles, can be followed by the following diffusion convection equation,

$$\frac{\partial g_e}{\partial t} + u \frac{\partial g_e}{\partial x} = \frac{1}{3} \frac{\partial u}{\partial x} \left(\frac{\partial g_e}{\partial y} - 4g_e \right) + \frac{\partial}{\partial x} \left[\kappa(x, y) \frac{\partial g_e}{\partial x} \right] + p \frac{\partial}{\partial y} \left(\frac{b_e}{p^2} g_e \right), \quad (1)$$

where $g_e = p^4 f_e$, $y = \ln(p/m_e c)$, m_e is the electron mass, c is the speed of light, and $\kappa(x, y)$ is the spatial diffusion coefficient (Skilling 1975).

Here, $b_e(p) = (4e^4/9m_e^4 c^6) B_{\text{eff}}^2 p^2$ represents the cooling of CR electrons due synchrotron and IC losses in cgs units, where e is the electron charge. The “effective” magnetic field strength, $B_{\text{eff}}^2 \equiv B^2 + B_{\text{CBB}}^2$, includes the equivalent strength of the cosmic background radiation with $B_{\text{CBB}} = 3.24 \mu\text{G}(1+z)^2$ at redshift z . The cooling time scale for electrons is given as

$$t_{\text{rad}}(\gamma_e) = \frac{p}{b_e(p)} = 9.8 \times 10^7 \text{ yrs} \left(\frac{B_{\text{eff}}}{5 \mu\text{G}} \right)^{-2} \left(\frac{\gamma_e}{10^4} \right)^{-1}, \quad (2)$$

where γ_e is the Lorentz factor of CR electrons.

The equation in (1) is solved using the test-particle version of the CRASH (Cosmic-Ray Amr SHock) code (see Kang et al. 2011, for details).

2.2. Models for Magnetic Field and Diffusion

Here, shocks are assumed to be gasdynamical for simplicity, that is, magnetic fields do not modify the background flow of the shock. In ICMs, magnetic fields of an inferred strength of order μG (Carilli & Taylor 2002; Govoni & Feretti 2004) are dynamically unimportant, since their energy density is less than $\sim 10\%$ of the thermal energy density (e.g., Ryu et al. 2008). However, magnetic fields, especially in the downstream region, are the key that governs DSA and the synchrotron cooling and emission of CR electrons. Theoretical studies have shown that efficient magnetic field amplification via resonant and non-resonant wave-particle interactions is an integral part of DSA at strong shocks (Lucek & Bell 2000; Bell 2004). In addition, magnetic fields can be amplified by turbulent motions behind shocks (Giagalone & Jokipii 2007; Inoue et al. 2009). Yet, these plasma processes are complex and their roles are not yet entirely certain, especially at weak shocks. So here we adopt a simple model in which the magnetic field strength is amplified by a constant factor of χ across the shock, that is, $B_2 = \chi B_1$. Hereafter, we use the subscripts ‘1’, and ‘2’ to label conditions in the preshock and postshock regions, respectively.

For κ , we adopt a Bohm-like diffusion coefficient with weaker non-relativistic momentum dependence,

$$\kappa(x, p) = \kappa^* \cdot \left(\frac{p}{m_e c} \right), \quad (3)$$

where $\kappa_1^* = m_e c^3 / (3e B_1) = 1.7 \times 10^{19} \text{ cm}^2 \text{ s}^{-1} (B_1 / 1 \mu\text{G})^{-1}$ in the preshock region and $\kappa_2^* = \kappa_1^* / \chi$ in the postshock region.

2.3. Injection of Electrons

As pointed in Introduction, the injection of electrons is expected to be much harder than that of protons in the so-called thermal leakage injection model. Because complex plasma interactions among CRs, waves, and the underlying gas flow are not fully understood, it is not yet possible to predict from first principles how particles are injected into the first-order Fermi process (e.g., Malkov & Drury 2001; Garat  & Spitkovsky 2012). In addition, postshock thermal electrons, which have gyro-radii smaller than those of thermal protons, need to be pre-accelerated to several times the peak momentum of thermal protons, $p_{\text{p,th}}$, before they can re-cross the shock transition layer. Here, $p_{\text{p,th}} = \sqrt{2m_p k_B T_2}$, where T_2 is the postshock gas temperature and k_B is the Boltzmann constant. Recently several authors have suggested pre-acceleration mechanisms based on plasma interactions with fluctuating magnetic fields that are locally quasi-perpendicular to the shock surface (e.g. Burgess 2006; Amano & Hoshino 2009; Guo & Giacalone 2010; Riquelme & Spitkovsky 2011). But the detailed picture of the

electron injection is not well constrained by plasma physics. Observationally, the ratio of CR electron number to proton number, $K_{e/p} \sim 0.01$, is commonly inferred for strong supernova remnant shocks, since about 1% of the Galactic CR flux near a GeV is due to electrons (Reynolds 2008). But this ratio is rather uncertain for weak shocks under consideration.

So here we adopt a simple model in which the postshock electrons above a certain injection momentum, $p_{\text{inj}} = Q_{\text{inj}} p_{\text{p,th}}$, are assumed to be injected to the CR population. Here, Q_{inj} is a parameter that depends on the shock Mach number and turbulent magnetic field amplitude in the thermal leakage injection model (Kang & Ryu 2010). The CR electron number density or, equivalently, the distribution function at p_{inj} at the shock location x_s , $f_e(x_s, p_{\text{inj}})$, will be scaled to match the observed flux of radio relics (see Sections 3.1 and 4.2).

2.4. Pre-existing CR Electrons

We consider the population of pre-existing CR electrons, along with that of freshly injected electrons at the shock. However, the nature of pre-existing CR electrons in ICMs is not well constrained. If they were generated at previous, external and internal shocks, a spectral slope of $s \sim 4.0 - 5.3$ is expected for $M \gtrsim 2$, close to the acceleration site. However, since their lifetime in equation (2) is much shorter than that of host clusters, it is unlikely that they are directly responsible for the pre-existing electron population we consider here. Any pre-existing CR electron should be locally produced, possibly either through $p - p$ collisions of CR protons with thermal protons or via turbulent re-acceleration of some populations (possibly including $p - p$ secondary electrons), as noted in Introduction. Petrosian & East (2008) have shown that turbulent injection of CR electrons from the thermal pool in ICMs is unlikely. The slope of protons re-accelerated by turbulence should be close to $s \sim 4$ (see, e.g., Chandran 2005), but that of electrons is strongly modified by coolings (Brunetti & Lazarian 2007, 2011). The slope of secondary electrons from $p - p$ collisions would be roughly $s \sim 4/3(s_p - 1)$ (Mannheim & Schlickeiser 1994), where s_p is the slope of CR protons, so typically, $s \sim 4 - 6$. In summary, pre-existing CR electrons may contain many different populations with different degrees of radiative cooling and may not be represented by a single power-law.

For simplicity, here we adopt a power-law form,

$$f_{e,1}(p) = f_{\text{pre}} \cdot \left(\frac{p}{p_{\text{inj}}} \right)^{-s}, \quad (4)$$

with slope s , as the model spectrum for pre-existing CR electrons. In modeling of specific radio relics, the value of s will be chosen as $s = 2\alpha_{\text{obs}} + 3$, where α_{obs} is the observed mean

spectral index. The amplitude, f_{pre} , is set by the ratio of upstream CR electron pressure to gas pressure, $R_1 \equiv P_{\text{CRE},1}/P_{\text{g},1}$. Here, R_1 is a parameter that will be scaled to match the observed fluxes of radio relics (see Sections 3.1 and 4.2).

3. ANALYTIC EVALUATIONS

We first consider some features in the CR electron energy spectrum and synchrotron emission spectrum for plane-parallel shocks, to provide analytic estimations for the simulation results presented in the next section.

3.1. Basic Features in CR Electron Spectrum

In the test-particle regime of DSA, the distribution of freshly injected and accelerated electrons at the “shock location” can be approximated, once it reaches equilibrium, by a power-law spectrum with super-exponential cutoff,

$$f_{e,2}(p) \approx f_{\text{inj}} \cdot \left(\frac{p}{p_{\text{inj}}} \right)^{-q} \exp \left(-\frac{p^2}{p_{\text{eq}}^2} \right), \quad (5)$$

where $q = 3\sigma/(\sigma - 1)$ (Kang 2011). In the case that $B_2 = \sigma B_1$, that is, the jump in the magnetic field strength across the shock is assumed to be same as the density jump, $\chi = \sigma$, and $\kappa_2 = \kappa_1/\sigma$, the cutoff momentum, which represents the balance between DSA and the radiative cooling, becomes

$$p_{\text{eq}} = \frac{m_e^2 c^2 u_s}{\sqrt{4e^3 q/27}} \left(\frac{B_1}{B_{\text{eff},1}^2 + B_{\text{eff},2}^2} \right)^{1/2}. \quad (6)$$

The corresponding Lorentz factor for typical merger shock parameters is then

$$\gamma_{e,\text{eq}} \approx 2 \times 10^9 q^{-1/2} \left(\frac{u_s}{3000 \text{ km s}^{-1}} \right) \left(\frac{B_1}{B_{\text{eff},1}^2 + B_{\text{eff},2}^2} \right)^{1/2}. \quad (7)$$

Hereafter, the magnetic field strength is given in units of μG . The acceleration time for electrons to reach p_{eq} , so the time for the equilibrium to be achieved, is estimated as

$$t_{\text{eq}} \approx (2.4 \times 10^4 \text{ yrs}) q^{1/2} B_1^{-1/2} (B_{\text{eff},1}^2 + B_{\text{eff},2}^2)^{-1/2} \left(\frac{u_s}{3000 \text{ km s}^{-1}} \right)^{-1}. \quad (8)$$

This is much shorter than the typical time scale of merger shocks, $\gtrsim 10^9$ yrs. For $t \gtrsim t_{\text{eq}}$, the DSA gains balance the radiative losses and the electron spectrum near the shock location asymptotes to a steady-state (Kang 2011).

With pre-existing CR electrons given in equation (4), the electrons distribution at the shock location can be written as the sum of the pre-existing/re-accelerated and freshly injected/accelerated populations,

$$f_{e,2}(p) \approx \begin{cases} \left[\frac{q}{(q-s)} \left(1 - \left(\frac{p}{p_{\text{inj}}} \right)^{-q+s} \right) f_{\text{pre}} \left(\frac{p}{p_{\text{inj}}} \right)^{-s} + f_{\text{inj}} \left(\frac{p}{p_{\text{inj}}} \right)^{-q} \right] \exp \left(-\frac{p^2}{p_{\text{eq}}^2} \right), & \text{when } s \neq q \\ \left[s \ln \left(\frac{p}{p_{\text{inj}}} \right) f_{\text{pre}} \left(\frac{p}{p_{\text{inj}}} \right)^{-s} + f_{\text{inj}} \left(\frac{p}{p_{\text{inj}}} \right)^{-q} \right] \exp \left(-\frac{p^2}{p_{\text{eq}}^2} \right), & \text{when } s = q. \end{cases} \quad (9)$$

(Kang & Ryu 2011). The relative importance of pre-existing to freshly injected populations depends on f_{pre} and f_{inj} , as well as on the slopes s and q in our model. For the sake of convenience, hereafter we will use the term “injected” electrons for those injected at the shock and then accelerated by DSA and the term “re-accelerated” electrons for those accelerated from the pre-existing population.

We here define the CR electron number fraction, $\xi_e \equiv n_{\text{CRe},2}/n_{e,2}$, as the ratio of CR electron number to thermal electron number in the postshock region. Here $n_{\text{CRe},2}$ includes CR electrons accelerated from both the pre-existing and freshly injected populations. Considering that the CR proton number fraction is likely to be $\xi_p \lesssim 10^{-4}$ at weak shocks (Kang & Ryu 2010) and $K_{e/p} \sim 0.01$, $\xi_e \sim 10^{-6}$ could be regarded as a canonical value. We note that the resulting radio emission is linearly scaled with both ξ_e and the preshock gas density, n_1 , in the test-particle regime, so the combined parameter, $n_1 \xi_e$, can be treated as a free parameter. We here fix the preshock gas density, $n_1 = 10^{-4} \text{cm}^{-3}$, as a fiducial parameter, but vary ξ_e to match the observed fluxes of radio relics. Another measure is the ratio of postshock CR electron pressure to gas pressure, $R_2 = P_{\text{CRe},2}/P_{g,2}$, which depends on both ξ_e and the slopes q and s . In modeling of specific radio relics in Section 4.2, we will determine the set of values for ξ_e , R_2 and R_1 , that matches the observed level of radio flux.

If we ignore for the moment the modest influence of continued DSA downstream of the shock, we can follow the electron population that advects downstream by solving the following equation :

$$\frac{dg_e}{dt} + V \cdot \frac{\partial g_e}{\partial y} = 0, \quad (10)$$

where $d/dt \equiv \partial/\partial t + u\partial/\partial x$ and $V = -b_e(p)/p = -Ce^y$. Here, $C = (4e^4/9m_e^4c^6)B_{\text{eff}}^2$ is a constant. This is basically the equation for downward advection in the space of $y = \ln(p/m_e c)$ due to radiative cooling. The general solution of the equation is

$$g_e(p, t) = G(e^{-y} - Ct) = G \left(\frac{p}{1 - t/t_{\text{rad}}} \right), \quad (11)$$

where $t_{\text{rad}} = 1/Ce^y$ is the electron cooling time scale. This provides the approximate distribution of CR electrons at the distance $d = u_2 t$ downstream from the shock, where u_2 is the downstream flow speed.

For instance, if the distribution function of the “injected” electrons at the shock location ($d = 0$) is the power-law spectrum, $g_e(p, 0) = g_{\text{inj}}(p/p_{\text{inj}})^{-q+4}$, the downstream spectrum can be approximated as

$$g_e(p, d) = g_{\text{inj}} \left[\frac{p}{(1 - d/u_2 t_{\text{rad}}) p_{\text{inj}}} \right]^{-q+4}. \quad (12)$$

It should be straightforward to apply the same approximation to the full spectrum given in equation (9). In Figures 1 and 2, we compare the distributions described by equation (11) with those from time-dependent DSA simulations, demonstrating that equation (11) provides reasonable approximations to the solutions of full DSA simulations (see Table 1 for specific model parameters).

3.2. Basic Features in Synchrotron Emission Spectrum

Since the synchrotron emission from mono-energetic electrons with γ_e has a broad peak around $\nu_{\text{peak}} \approx 0.3(3eB/4\pi m_e c)\gamma_e^2$, for a given observation frequency, ν_{obs} , the greatest contribution comes from electrons of the Lorentz factor,

$$\gamma_{e,\text{peak}} \approx 1.26 \times 10^4 \left(\frac{\nu_{\text{obs}}}{1\text{GHz}} \right)^{1/2} \left(\frac{B}{5 \mu\text{G}} \right)^{-1/2} (1+z)^{1/2}. \quad (13)$$

Using equations (2) and (13), the cooling time of the electrons emitting at ν_{obs} can be estimated approximately as

$$t_{\text{rad}} \approx 8.7 \times 10^8 \text{ yrs} \left(\frac{B_2^{1/2}}{B_{\text{eff},2}^2} \right) \left(\frac{\nu_{\text{obs}}}{1\text{GHz}} \right)^{-1/2} (1+z)^{-1/2}. \quad (14)$$

The cooling length behind the shock, $u_2 t_{\text{rad}}$, then becomes

$$L_{\text{rad}} \approx 890 \text{ kpc} \left(\frac{u_2}{10^3 \text{ km s}^{-1}} \right) \left(\frac{B_2^{1/2}}{B_{\text{eff},2}^2} \right) \left(\frac{\nu_{\text{obs}}}{1\text{GHz}} \right)^{-1/2} (1+z)^{-1/2}. \quad (15)$$

Note that $B_{\text{eff},2}^2/B_2^{1/2} \sim 15 - 25$ for the model parameters considered here. Again, t_{rad} is shorter than the typical time scale of merger shocks, $\gtrsim 10^9$ yrs. So L_{rad} should represent the width of radio emitting region at ν_{obs} behind plane-parallel shocks. In radio relics, however, the observed width is constrained by both L_{rad} and the projection angle of spherical shocks (see Section 4.2).

The cutoff energy in the electron spectrum due to the radiative cooling decreases linearly with the distance from the shock location, that is, $\gamma_{e,\text{cut}} \propto d^{-1}$, as expected from equation

(2) and shown in Figure 1. At the farthest downstream point, $d = u_2 t$, where t is the shock age, the cutoff energy becomes

$$\gamma_{e,\text{br}}(t) \approx 9.82 \times 10^2 \left(\frac{t}{10^9 \text{ yrs}} \right)^{-1} \left(\frac{B_{\text{eff},2}}{5 \mu\text{G}} \right)^{-2}. \quad (16)$$

If the electron distribution function at the shock location has a power-law form, $n_e(x_s, \gamma_e) \propto \gamma_e^{-r}$, then the volume-integrated electron spectrum downstream steepens by the power-law index of one, *i.e.*, $N_{e,2} \propto \gamma_e^{-(r+1)}$ for $\gamma_e > \gamma_{e,\text{br}}$. It is because the width of the spatial distribution of electrons with γ_e decreases as γ_e^{-1} (Zirakashvili & Aharonian 2007; Kang 2011). As a consequence, the “volume-integrated” synchrotron spectrum from aged electrons has a spectral break, *i.e.*, an increase of the spectral index α by +0.5, at

$$\nu_{\text{br}} = 0.3 \frac{3}{4\pi} \frac{e B_2}{m_e c} \gamma_{e,\text{br}}^2 \approx 6.1 \times 10^6 \text{ Hz} \left(\frac{t}{10^9 \text{ yrs}} \right)^{-2} \left(\frac{B_2}{5 \mu\text{G}} \right) \left(\frac{B_{\text{eff},2}}{5 \mu\text{G}} \right)^{-4}. \quad (17)$$

So the shock age may be estimated from the break frequency ν_{br} , if the magnetic field strength is known.

4. RESULTS OF DSA SIMULATIONS

4.1. Plane-Parallel Shocks

The model parameters of our simulations for plane-parallel shocks are summarized in Table 1. Here, z is the redshift, $c_{s,1}$ is the preshock sound speed, M is the shock Mach number, u_2 is the postshock flow speed, s is the power-law slope of pre-existing CR electrons, and B_2 is the postshock magnetic field strength. The model name in the first column includes the values of M , B_2 , and s ; for models without pre-existing CRs, “I” (injection only) is specified. For instance, M4.5B7I stands for the model with $M = 4.5$, $B_2 = 7 \mu\text{G}$, and injected CR electrons only (no pre-existing CRs), while M2B2.3S4.2 stands for the model with $M = 2.0$, $B_2 = 2.3 \mu\text{G}$, and $s = 4.2$. For the preshock magnetic field strength, $B_1 = 1 \mu\text{G}$ is adopted for all models, which is close to the typical quoted value in cluster outskirts (see Brüggen et al. 2011, and references therein). Once $B_1 < B_{\text{CBB}}$, the IC cooling dominates, and the exact value of B_1 is not important in our models. The model parameters are chosen to match the observed properties of radio relics in clusters CIZA J2242.8+5301 and ZwCl 0008.8+5215 (see the next subsection for details). For example, $M = 4.5$ or $s = 4.2$ is chosen to match the observed spectral index, $\alpha = 0.6$, of the relic in CIZA J2242.8+5301, and $M = 2$ or $s = 5.4$ is chosen to match $\alpha = 1.2$ of the relic in ZwCl 0008.8+5215. For reference, the shock compression ratio is $\sigma = 3.5$ for $M = 4.5$ and $\sigma = 2.3$ for $M = 2$. The values of u_2 and

B_2 are chosen to match the observed width of the relics, since they determine the cooling length as shown in equation (15).

Figure 1 shows the CR electron distribution at different locations downstream of the shock, after it has reached the steady state, for M4.5B3.5I, M2B7S4.2, M2B2.3I and M2B2.3S5.4 models. For the comparison of different models, here the postshock CR electron number fraction is set to be $\xi_e = 10^{-6}$, which sets the vertical amplitude. The injection-only models exhibit the power-law distributions with cutoffs due to the cooling, as discussed in the previous section. In M2B7S4.2 model, the electrons accelerated from the injected population are important only at low energies ($\gamma_e \lesssim 10^{2.5}$) and they dominate in terms of particle number, because the “injected” spectrum is much softer than the “re-accelerated” spectrum (i.e. $q > s$). The electrons accelerated from the pre-existing population, on the other hand, dominate at higher energies including $\gamma_e \sim 10^4$ and they are most relevant for the synchrotron emission at $\nu \sim 1$ GHz. The slope of the accelerated spectrum at high energies is similar to that of the pre-existing spectrum, which is consistent with equation (9). On the contrary, in M2B2.3S5.4 model with $s \approx q$, the “injected” electrons are negligible even at low energies. This difference comes about, because with similar numbers of pre-existing CRs, the amplitude f_{pre} is larger in M2B2.3S5.4 (with $s = 5.4$) than in M2B7S4.2 (with $s = 4.2$). The numbers of injected electrons should be similar in the two models, because the shock Mach number is the same. Note that the re-accelerated spectrum flattens by a factor of $\ln(p)$, as shown in equation (9), because $s \approx q$ in this model.

The left column of Figure 2 shows the spatial profile of the electron distribution function, $g_e(\gamma_e, x)$, at two specific energies (γ_e) as a function of the downstream distance for the M4.5B7I, M4.5B3.5I and M2B7S4.2 models. For each model the Lorentz factors are calculated for $\nu_{\text{obs}} = 0.61$ GHz and 2.3 GHz according to equation (13). The upper/lower curves represent g_e of the lower/higher values of γ_e , respectively. The right column of Figure 2 shows the synchrotron emission, $j_\nu(x)$, at $\nu_{\text{obs}} = 0.61$ GHz (upper curves) and 2.3 GHz (lower curves). The solid lines show g_e and j_ν calculated from the DSA simulation results, while the dashed lines show the approximate solutions calculated with equation (11). The figure demonstrates that the lower energy electrons advect further from the shock before cooling than higher energy electrons, so the lower-frequency radio emission has larger widths than the higher-frequency one. According to equation (15), the cooling lengths of the electrons emitting at 0.61 and 2.3 GHz are $L_{\text{rad}} \approx 40$ and 20 kpc, respectively, in the three models.

4.2. Modeling of Radio Relics

As noted above, it should be sufficient to employ the plane shock approximation to compute the distributions of CR electrons and their emissivities as a function of the distance from the shock surface. In observed radio relics, however, radio emitting shells are likely to be curved with finite curvatures along the observer’s line of sight (LoS) as well as in the plane of the sky. So in modeling of radio relics, the curved shell needs to be projected onto the plane of the sky. In that case LoS’s from the observer will transect a range of shock displacements, and this needs to be taken into account when computing the observed brightness distribution of model relics. Following the approach of van Weeren et al. (2010, 2011), we consider a piece of a spherical shell with outer radius R_s , subtended along the LoS from $+\psi$ to $-\psi$ so for the total angle of 2ψ . Then, R_s and the projection angle ψ are the parameters that fix the shape of the curved shell to be projected onto the plane of the sky. The synchrotron emissivity, j_ν ($\text{erg cm}^{-3} \text{ s}^{-1} \text{ Hz}^{-1} \text{ str}^{-1}$), at each point behind the curved shock is approximated as that downstream of plane-parallel shocks discussed in the previous subsection. Since we do not consider the polarization of synchrotron emissions here, so, for simplicity, the magnetic field lines are assumed to lie in the plane of the sky; that is, the angle between the magnetic field vectors and the LoS is fixed at 90° .

The synchrotron intensity is calculated by integrating the emissivity along the LoS, $I_\nu(r) = \int j_\nu dl$ ($\text{erg cm}^{-2} \text{ s}^{-1} \text{ Hz}^{-1} \text{ str}^{-1}$), where r is the distance behind the projected shock edge in the plane of the sky. The bound of the path length, l , for given r is determined by R_s and ψ . Then, the observed flux is estimated, assuming a Gaussian beam with e-width, θ , as

$$S_\nu(r) \approx I_\nu(r) \pi \theta^2 (1+z)^{-3}, \quad (18)$$

where $\nu = \nu_{\text{obs}}(1+z)$.

Figure 3 shows the profiles of the synchrotron flux, $S_\nu(r)$, at $\nu_{\text{obs}} = 0.61$ GHz (left column) and the spectral index, $\alpha = -d \ln S_\nu / d \ln \nu$, estimated with the fluxes at $\nu_{\text{obs}} = 0.61$ and 1.4 GHz (right column) for the M4.5B7I, M4.5B3.5I and M2B7S4.2 models, which are designed to reproduce the radio relic in CIZA J2242.8+5301. The flux is calculated with the beam of $\theta^2 = \theta_1 \theta_2 / (4 \ln 2)$, $\theta_1 \theta_2 = 16.7'' \times 12.7''$. They are compared with the “deconvolved” profile of observed flux taken from Figure 4 of van Weeren et al. (2010) (filled circles). Since the observed flux is given in an arbitrary unit in their paper, we scale it so that the peak value of $S_\nu(r)$ becomes 5 mJy, which is close to the observed value (private communication with R. J. van Weeren). The radius of the spherical shock is set to be $R_s = 1.5$ Mpc and two values of projection angle, $\psi = 10^\circ$ and 20° , are considered. The observed profile is well fitted by the three models, if $\psi = 10^\circ$ is taken. In M4.5B7I and M4.5B3.5I, different values of u_2 are assumed to match the observed width (see Table 1). The observed value

of the spectral index at $r = 0$, $\alpha = 0.6$, is reproduced either in the injection-only models with $M = 4.5$ or in the model with pre-existing CRs with the slope $s = 4.2$, as noted in the previous subsection.

For the fiducial preshock particle density of $n_1 = 10^{-4} \text{ cm}^{-3}$, the values of the postshock electron CR number fraction required to match the peak flux of 5 mJy are $\xi_e = 7.6 \times 10^{-8}$, 2.3×10^{-7} , and 2.6×10^{-7} for M4.5B7I, M4.5B3.5I, and M2B7S4.2, respectively. In M2B7S4.2 model the ratio of the pressure of pre-existing CR electrons to gas pressure far upstream is $R_1 \sim 6.7 \times 10^{-5}$. Those values of ξ_e and R_1 are modest enough that they probably are not in conflict with the values expected in clusters. Our results demonstrate that if the pre-existing electron population is considered, the radio relic in CIZA J2242.8+5301 can be reproduced even with weak shocks of $M \sim 2$ or so. We note that R_1 is a model parameter that sets the amplitude, f_{pre} , of the upstream population, while the fraction ξ_e is the outcome of DSA of both pre-existing and injected electrons. As noted in Figure 1, in M2B7S4.2 model the fraction ξ_e is determined mostly by the “injected” population at low energies, while the radio emission is regulated mostly by the “re-accelerated” population at $\gamma_e \sim 10^4$. So we should obtain the similar radio flux even with a much lower injection rate for this model, and the resulting ξ_e could be much smaller than the current value of 2.6×10^{-7} .

We point that the radio relic in CIZA J2242.8+5301 is subtended in the plane of the sky over the angle of $\sim 60 - 70^\circ$. This means that the surface of the shock responsible for the relic should be highly elongated with the aspect ratio of $\sim (60 - 70^\circ)/(2\psi) = \sim 3 - 3.5$ when $\psi = 10^\circ$ is adopted. It would not be trivial, if not impossible, for such structure to be induced in merger events in clusters. Or the relic may actually consist of a number of substructures, which is hinted by the variations in the observed flux profile along the arc in the plane of the sky.

The left column of Figure 4 shows the synchrotron flux profiles at $\nu_{\text{obs}} = 1.38 \text{ GHz}$, for M2B2.3I and M2B2.3S5.4 models, which are designed to reproduce the radio relic in ZwCl008.8+5215. The flux is calculated with $\theta^2 = \theta_1\theta_2/(4 \ln 2)$, $\theta_1\theta_2 = 23.5'' \times 17.0''$. We note that this beam size is fine enough that the convolved profiles with a Gaussian beam (dotted and long-dashed lines) are very similar to the unconvolved profiles (solid lines). The profiles are compared with the observed profile given in Figure 16 of van Weeren et al. (2011) (filled circles). Again the observed flux is given in an arbitrary unit, so it is scaled at 5 mJy at the peak. The right column shows the profiles of α , estimated with fluxes at $\nu_{\text{obs}} = 0.24$ and 1.38 GHz, along with the observed α also taken from Figure 16 of van Weeren et al. (2011) (filled circles). The shock radius is assumed to be $R_s = 1.0 \text{ Mpc}$ and two values of projection angle, $\psi = 25^\circ$ and 30° , are considered. The two models shown are the same except the existence of pre-existing CR electrons in M2B2.3S5.4 model. In M2B2.3S5.4, the

“re-accelerated” population dominates over the “injected” population. Yet, the two models give similar profiles of S_ν and α . We see that in our models $\psi = 30^\circ$ gives good fits to the observed profiles of S_ν and α , while van Weeren et al. (2011) argued that $\psi = 22^\circ$ seems to give a reasonable fit. Note that they adopted $u_2 = 750 \text{ km s}^{-1}$ and $B_2 = 2 \text{ } \mu\text{G}$, giving $L_{\text{rad}} = 40 \text{ kpc}$, while in our models $u_2 = 1100 \text{ km s}^{-1}$ and $B_2 = 2.4 \text{ } \mu\text{G}$, giving $L_{\text{rad}} = 57 \text{ kpc}$.

For the assumed value of $n_1 = 10^{-4} \text{ cm}^{-3}$, the postshock CR electron number fraction required to match the peak flux of 5 mJy is $\xi_e = 2.1 \times 10^{-4}$ for M2B2.3I, which is six times larger than $\xi_e = 3.3 \times 10^{-5}$ for M2B2.3S5.4. This is because the spectral shapes of CR electron spectrum below $\gamma_e \lesssim 10^{2.5}$ are different in the two models (see Fig. 1 and discussion in the previous subsection). The number fraction of CR electrons for M2B2.3I seems too large, considering that the postshock proton CR number fraction is likely to be $\xi_p \lesssim 10^{-4}$ for $M = 2$ (Kang & Ryu 2010). In M2B2.3S5.4, on the other hand, the ratio of upstream CR electrons pressure to gas pressure is $R_1 \sim 1.2 \times 10^{-3}$. This seems to be marginal, that is, not inconsistent with expected values, considering that the ratio of CR proton pressure to gas pressure is $\lesssim 10^{-2} - 10^{-1}$ in ICMs as noted in Introduction. But we should point that the values of ξ_e and R_1 in these two models are dominated by low-energy CR electrons with $\gamma_e \lesssim 10^3$ (see Figure 1), which do not contribute much to the synchrotron radiation observed in radio relics. So if the “injected” population in M2B2.3I consists of electrons with $\gamma_e \gtrsim 10^3$ only, the required values of ξ_e could be reduced by a factor of ~ 10 , easing down the constraint. Since we do not understand fully the plasma interactions involved in the pre-acceleration and injection of electrons at the shock, the detailed spectral shape of those low energy electrons are very uncertain.

The top panels of Figure 5 show the profiles of the intensity, $I_\nu(r) = \int j_\nu dl$, at 6 cm (5 GHz), 20 cm (1.5 GHz), and 91 cm (0.33 GHz) in arbitrary units as a function of r for the M4.5B3.5I, M2B7S4.2 and M2B2.3I models. Here, the projection angle is set to be $\psi = 30^\circ$. Since the emissivity j_ν decreases downstream of the shock, while the path length increases with r , the profiles of I_ν exhibit non-monotonic behaviors. For example, the profiles at 6 cm show a slightly concave turnover before it decreases abruptly at $r \approx 200 \text{ kpc}$. The middle panels show the spectral indices, α_{20}^6 (solid lines) calculated between 6 and 20 cm and α_{91}^{20} (dashed lines) calculated between 20 and 91 cm, when the projection angle is set to be $\psi = 10^\circ, 20^\circ$ and 30° . The general trend is the increase of α_{20}^6 and α_{91}^{20} as we move away from the projected shock edge at $r = 0$, reflecting the effects of radiative cooling. Also $\alpha_{20}^6 > \alpha_{91}^{20}$, that is, the slope is steeper at higher frequencies. The bottom panels show the color-color diagram of α_{91}^{20} versus α_{20}^6 . The rightmost point ($\alpha_{20}^6 = \alpha_{91}^{20} = \alpha_s$) corresponds to the projected shock edge. Away from the edge, the loci move towards the lower left direction. In both middle and bottom panels, the spectral slopes also show a slightly

concave turnover for large projection angles of $\psi = 20^\circ$ and 30° . Recently, van Weeren et al. (2012) reported the color-color diagram for the so-called “Toothbrush” relic in cluster 1RXS J0603.3+4214, which shows a spectral behavior that is consistent with the cooled electron population downstream of the shock.

5. SUMMARY

In an effort to refine our understandings of radio relics in clusters of galaxies, we have performed time-dependent, DSA simulations of CR electrons and calculated the synchrotron emission from CR electrons for plane-parallel shocks. The energy losses due to synchrotron and IC have been explicitly included. Weak shocks expected to be found in ICMs have been considered. Both the cases with and without pre-existing CR electrons have been considered. The relevant physics of DSA and cooling is well represented by plane-parallel shocks, since the time scales over which electrons are accelerated and cool are much shorter than the lifetime of merger shocks in clusters and the radio emission is confined to a region of small width behind the shock front. We then have modeled the synchrotron flux and spectral distributions from spherical shocks by approximating them with plane-parallel shocks and projecting to the plane of the sky for the angle from $+\psi$ to $-\psi$ along the LoS. For the specific models which are designed to reproduce radio relics in clusters CIZA J2242.8+5301 and ZwCl0008.8+5215, we have compared the resulting distributions with observed ones in details.

The main results are summarized as follows:

1) The CR electron spectrum becomes steady, after the DSA gains balance the radiative losses. The spectrum at the shock location is well approximated by a distribution with super-exponential cutoff at p_{eq} , $f_{e,2}(p) \propto \exp(-p^2/p_{\text{eq}}^2)$. The full expressions of $f_{e,2}(p)$ and p_{eq} are given in equations (9) and (6).

2) The spectrum of the downstream CR electrons that have cooled for the advection time, $t = d/u_2$, can be approximated with $g_e(p, d) = G[p/(1 - d/u_2 t_{\text{rad}})]$ at the distance d from the shock location. Here, G is the functional form of the spectrum at the shock location of $d = 0$. The synchrotron emission from this analytic formula provides a reasonable approximation to that calculated using DSA simulation results (see Figure 2).

3) Both the models of $M = 4.5$ shock without pre-existing CR electrons and $M = 2$ shock with pre-existing CR electrons of $f_{e,1} \propto p^{-4.2}$ may explain the observed properties of the radio relic in CIZA J2242.8+5301. The postshock electron CR number fraction of $\xi_e \sim 10^{-7}$ in the injection-only model or the ratio of upstream CR electrons pressure to gas

pressure of $R_1 \sim \text{several} \times 10^{-5}$ in the model with pre-existing CRs are required to explain the observed radio flux of several mJy. Those values of ξ_e and R_1 are modest enough to be accommodated in typical clusters. But the surface of the shock responsible for the relic should be highly elongated with the aspect ratio of $\sim 3 - 3.5$. It would not be trivial for such structure to be induced in merger events in clusters.

4) The radio relic in ZwCl0008.8+5215 may be explained by the models of $M = 2$ shock with or without pre-existing CR electrons. However, in the injection-only model, $\xi_e \gtrsim 10^{-4}$, required to explain the observed radio flux of several mJy, is probably too large for the weak shock of $M = 2$. On the other hand, in the model with pre-existing CRs, $R_1 \sim 10^{-3}$, required to explain the observed flux, seems to be marginal, that is, not inconsistent with expected values in clusters. In the model, then, the origin of such pre-existing electron population is an important topic, but beyond the scope of the present paper.

5) The color-color diagram of α_{91}^{20} vs α_{20}^6 has been presented behind the projected shock edge. It includes an important information about the evolutionary properties of the post-shock electrons. Due to the effect of the projection with limited subtended angle along the LoS for spherical shocks, the diagram behaves differently for different projection angles. So it may provide an independent way to estimate the projection angle, which is a key parameter in modeling of radio relics.

HK was supported by Basic Science Research Program through the National Research Foundation of Korea funded by the Ministry of Education, Science and Technology (2011-0002433). DR was supported by the National Research Foundation of Korea through grant 2007-0093860. TWJ was supported by NASA grant NNX09AH78G, NSF grant AST-0908668 and by the Minnesota Supercomputing Institute for Advanced Computational Research. We thanks R. J. van Weeren and L. Rudnick for discussions.

REFERENCES

- Abdo, A. A. et al. 2010, *Science*, 327, 1103
- Akamatsu, H., & Kawahara, H. 2011, preprint, arXiv:1112.3030A
- Alaksić, E. et al. 2012, preprint, arXiv:1111.5544
- Amano, T., Hoshino, M., & Kawahara, H. 2009, *ApJ*, 690, 244
- Arlen, T. et al. 2012, preprint

- Bell, A. R. 1978, MNRAS, 182, 147
- Bell, A. R. 2004, MNRAS, 353, 550
- Blasi, P. 2010, MNRAS, 402, 2807
- Brüggen, M., Bykov, A., Ryu, D., & Röttgering, H. 2012, Space Sci. Rev., Online First (10.1007/s11214-011-9785-9)
- Brunetti, G., & Lazarian, A. 2007, MNRAS, 378, 245
- Brunetti, G., & Lazarian, A. 2011, MNRAS, 412, 817
- Burgess, D. 2006, ApJ, 653, 316
- Carilli, C. L., & Taylor, G. B. 2002, ARA&A, 40, 319
- Chandran, B. D. G. 2005, Phys. Rev. Lett., 95, 265004
- Donnert, J., Dolag, K., Cassano, R., & Brunetti, G. 2010, MNRAS, 407, 1565
- Drury, L. O’C. 1983, Rept. Prog. Phys., 46, 973
- Enßlin, T. A., Biermann, P. L., Klein, U., & Kohle, S. 1998, A&A, 332, 395
- Ferrari, C., Govoni, F., Schindler, S., Bykov, A. M., & Rephaeli Y. 2008, Space Sci. Rev., 134, 93
- Finoguenov, A., Sarazin, C. L., Nakazawa, K. Wik, D. R., & Clarke, T. E. 2010, ApJ, 715, 1143
- Garaté L., & Spitkovsky, A. 2012, ApJ, 744, 67
- Giacalone, J., & Jokipii, J. R. 2007, ApJ, 663, L41
- Guo, F., & Giacalone, J. 2010, ApJ, 715, 406
- Govoni, F., & Feretti, L. 2004, Int. J. Mod. Phys. D, 13, 1549
- Hoeft, M., Brüggen, M., Yepes, G., Gottlober, S., & Schwobe, A. 2008, MNRAS, 391, 1511
- Inoue, T., Yamazaki, R., & Inutsuka, S. 2009, ApJ, 695, 825
- Kang, H. 2011, Journal of Korean Astronomical Society, 44, 39
- Kang, H., Edmon, P. P., & Jones, T. W. 2011, ApJ, in press

- Kang, H., & Ryu, D. 2010, ApJ, 721, 886
- Kang, H., & Ryu, D. 2011, ApJ, 734, 18
- Kang, H., Ryu, D., Cen, R., & Ostriker, J. P. 2007, ApJ, 669, 729
- Lucek, S. G., & Bell, A. R. 2000, MNRAS, 314, 65
- Malkov M. A., & Drury, L. O’C. 2001, Rep. Prog. Phys., 64, 429
- Mannheim, K., & Schlickeiser, R. 1994, A&A, 286, 983
- Miniati, F., Ryu, D., Kang, H., Jones, T. W., Cen, R., & Ostriker, J. P. 2000, ApJ, 542, 608
- Miniati, F., Jones, T. W., Kang, H., & Ryu, D. 2001, ApJ, 562, 233
- Nuza, S. E., Hoeft, M., van Weeren, R. J., Gottlöber, S., & Yepes, G. 2012, MNRAS, 420, 2006
- Petrosian, V., & East, W. E. 2008, ApJ, 682, 175
- Pfrommer, C., & Enßlin, T. A. 2004, A&A, 413, 17
- Pfrommer, C., Springel, V., Enßlin, T. A., & Jubelgas, M. 2006, MNRAS, 367, 113
- Reynolds, S. P. 2008, ARA&A, 493, 375
- Riquelme, M. A., & Spitkovsky, A. 2011, ApJ, 733:63
- Roettiger, K., Burns, J. O., & Stone, J. M. 1999, ApJ, 518, 603
- Ryu, D., Kang, H., Cho, J., & Das, S. 2008, Science, 320, 909
- Ryu, D., Kang, H., Hallman, E., & Jones, T. W. 2003, ApJ, 593, 599
- Skilling, J. 1975, MNRAS, 172, 557
- Skillman, S. W., Hallman, E. J., O’Shea, W., Burns, J. O., Smith, B. D., & Turk, M. J. 2011, ApJ, 735, 96
- Skillman, S. W., O’Shea, B. W., Hallman, E. J., Burns, J. O., & Norman, M. L. 2008, ApJ, 689, 1063
- van Weeren, R., Hoeft, M., Röttgering, H. J. A., Brüggen, M., Intema, H. T., & van Velzen, S. 2011, A&A, 528, A38

- van Weeren, R., Röttgering, H. J. A., Brüggen, M., & Hoeft, M. 2010, *Science*, 330, 347
- van Weeren, R., Röttgering, H. J. A., Intema, H. T., Rudnick, L., Brüggen, M., Hoeft, M., & Oonk, J. B. R. 2012, *A&A*, submitted
- Vazza, F., Brüggen, M., van Weeren, R., Bonafede, A., Dolag, K., & Brunetti, G. 2012, *MNRAS*, 421, 1868
- Vazza, F., Brunetti, G., & Gheller, C. 2009, *MNRAS*, 395, 1333
- Zirakashvili V. N., & Aharonian F. A. 2007, *A&A*, 465, 695

Table 1. Parameters for Plane-Parallel Shock Simulations

Model Name	z	$c_{s,1}$ (km s ⁻¹)	M	u_2 (km s ⁻¹)	s	B_2 (μ G)	Cluster
M4.5B7I	0.1921	7.8×10^2	4.5	1.0×10^3	-	7.0	CIZA J2242.8+5301
M4.5B3.5I	0.1921	6.0×10^2	4.5	7.7×10^2	-	3.5	CIZA J2242.8+5301
M2B2.3S4.2	0.1921	1.25×10^3	2.0	1.1×10^3	4.2	2.3	CIZA J2242.8+5301
M2B7S4.2	0.1921	1.25×10^3	2.0	1.1×10^3	4.2	7.0	CIZA J2242.8+5301
M2B2.3I	0.103	1.25×10^3	2.0	1.1×10^3	-	2.3	ZwCl0008.8+5215
M2B2.3S5.4	0.103	1.25×10^3	2.0	1.1×10^3	5.4	2.3	ZwCl0008.8+5215

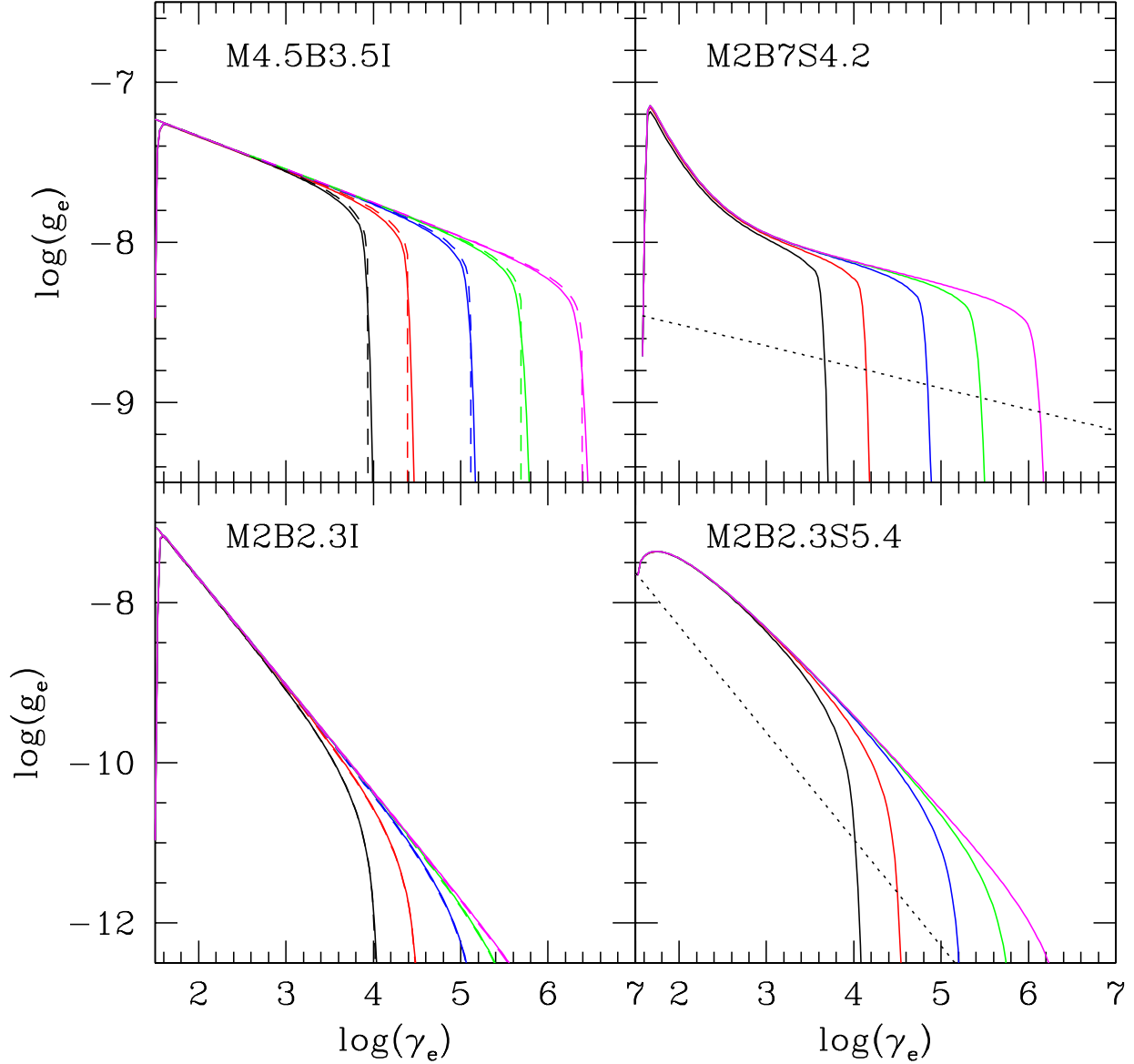


Fig. 1.— The distribution function, $g_e = f_{e,2}(\gamma_e)\gamma_e^4$, of CR electrons at 5 different locations downstream of the shock for the M4.5B3.5I, M2B7S4.2, M2B2.3I, and M2B2.3S5.4 models (see Table 1 for model parameters). In this figure the postshock CR electron number fraction is set to be $\xi_e = 10^{-6}$ for comparison of the models. In all the models, solid lines are the results of DSA simulations. In M4.5B3.5I and M2B2.3I, dashed lines show the approximate solution given in equation (11). In M2B7S4.2 and M2B2.3S5.4, the distribution of the pre-existing population of CR electrons is shown with dotted lines. The five downstream locations are: $d = 0.30, 1.4, 5.8, 29, 86$ kpc in M4.5B3.5I, $d = 0.34, 1.7, 6.1, 34, 100$ kpc in M2B7S4.2, $d = 0.42, 2.0, 8.1, 40, 120$ kpc in M2B2.3I and M2B2.3S4.2.

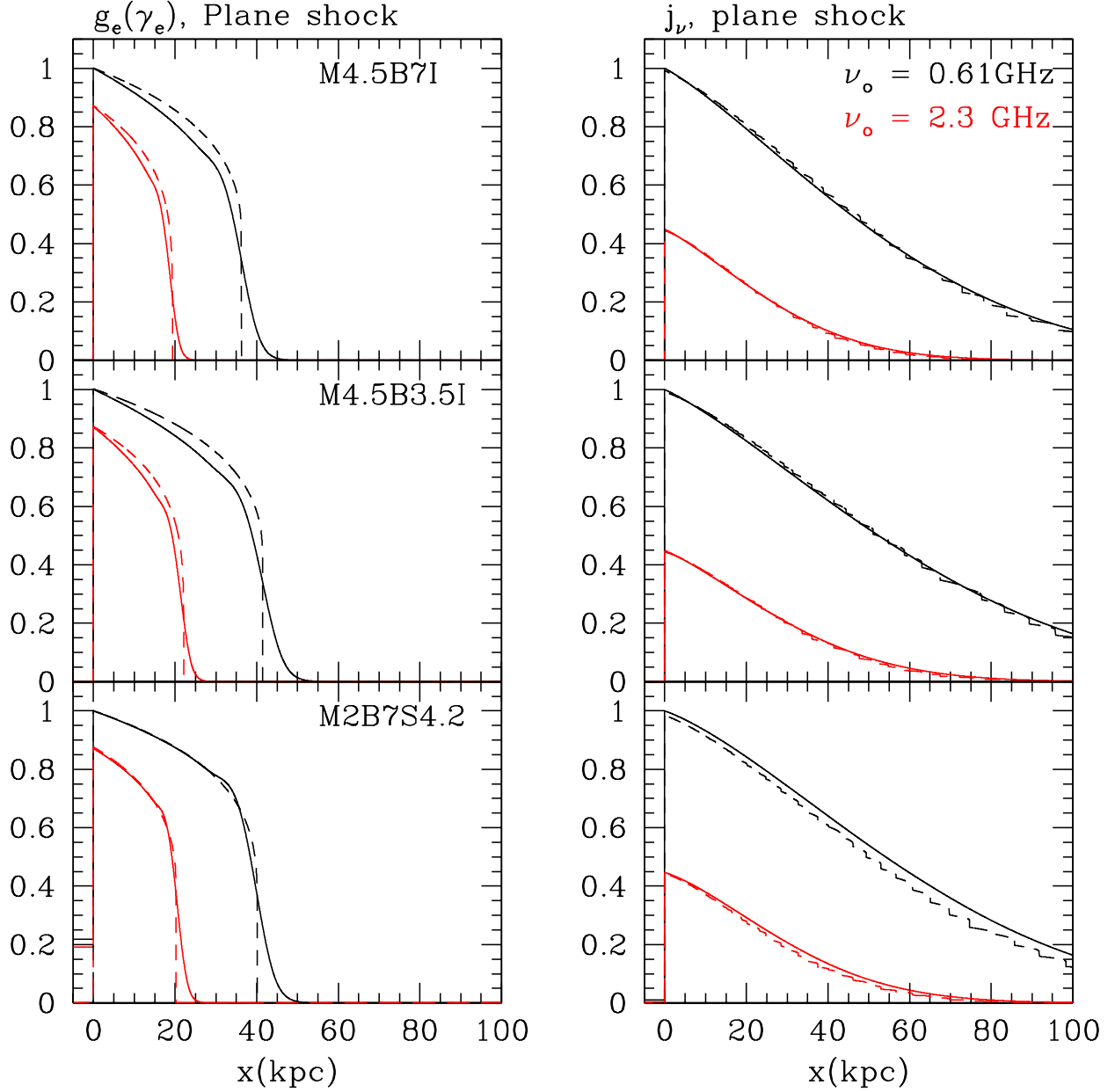


Fig. 2.— Left: The distribution function, $g_e(x)$, of CR electrons with γ_e 's given in equation (13) for $\nu_{\text{obs}} = 0.61$ and 2.3 GHz in the downstream region for the M4.5B7I, M4.5B3.5I, and M2B7S4.2 models. Right: The synchrotron emissivity, $j_\nu(x)$, at $\nu_{\text{obs}} = 0.61$ and 2.3 GHz for the same three models. Solid lines are the results of DSA simulations, and dashed lines show the approximate solution given in equation (11) and the emissivity calculated using the solution.

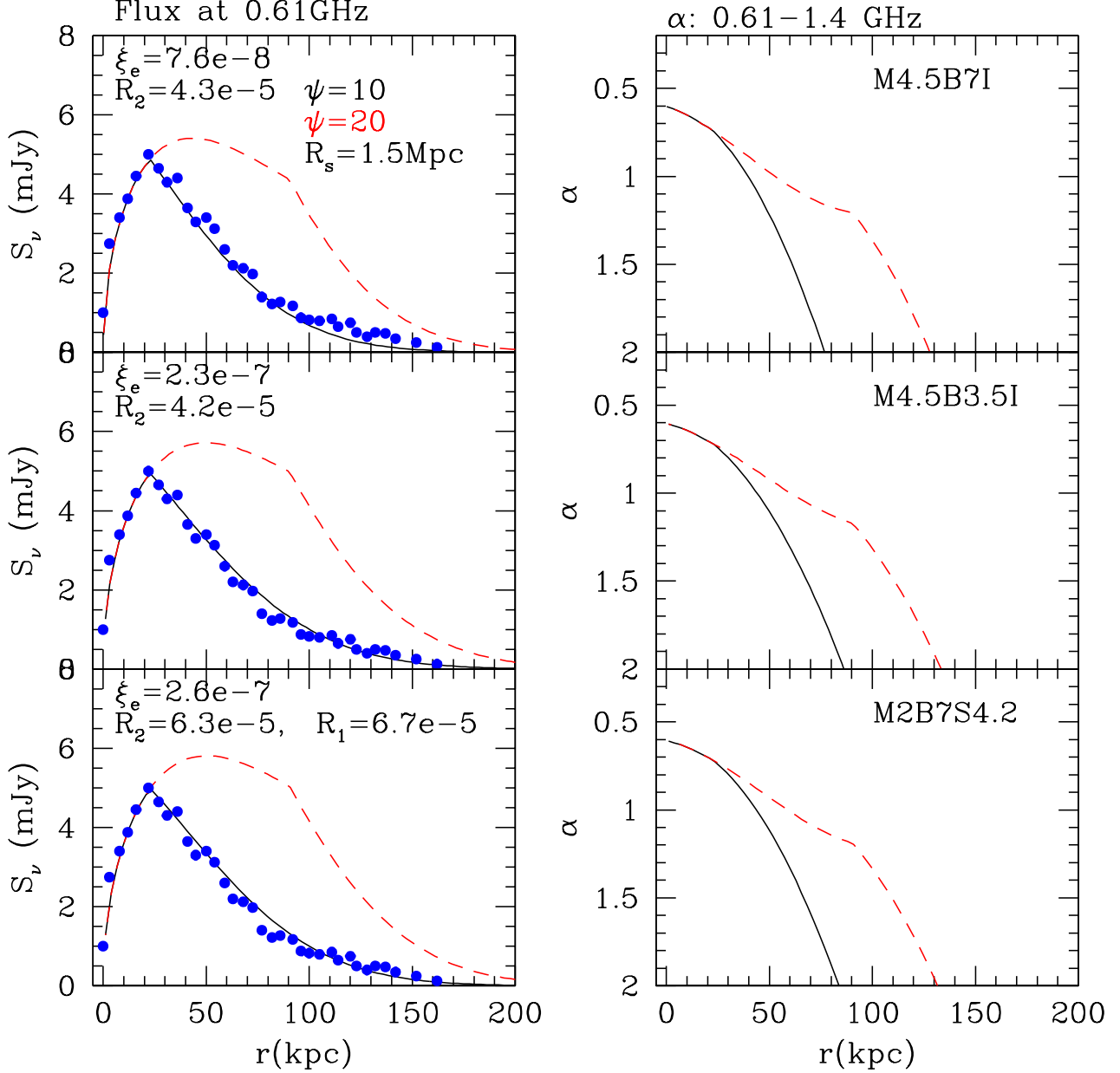


Fig. 3.— The synchrotron flux, S_ν , at 0.61GHz and the spectral index, α , between 0.61 GHz and 1.4 GHz for the M4.5B7I, M4.5B3.5I, and M2B7S4.2 models. Spherical shocks with radius $R_s = 1.5$ Mpc are assumed, and two projection angles, $\psi = 10^\circ$ (solid lines) and 20° (dashed lines), are considered. Filled circles are the data points taken from van Weeren et al. (2010) for the radio relic in CIZA J2242.8+5301. The flux is scaled so that the peak has 5 mJy. The required values of the postshock electron CR number fraction, ξ_e , and the ratio of upstream and downstream CR electrons pressure to gas pressure, R_1 and R_2 , are shown.

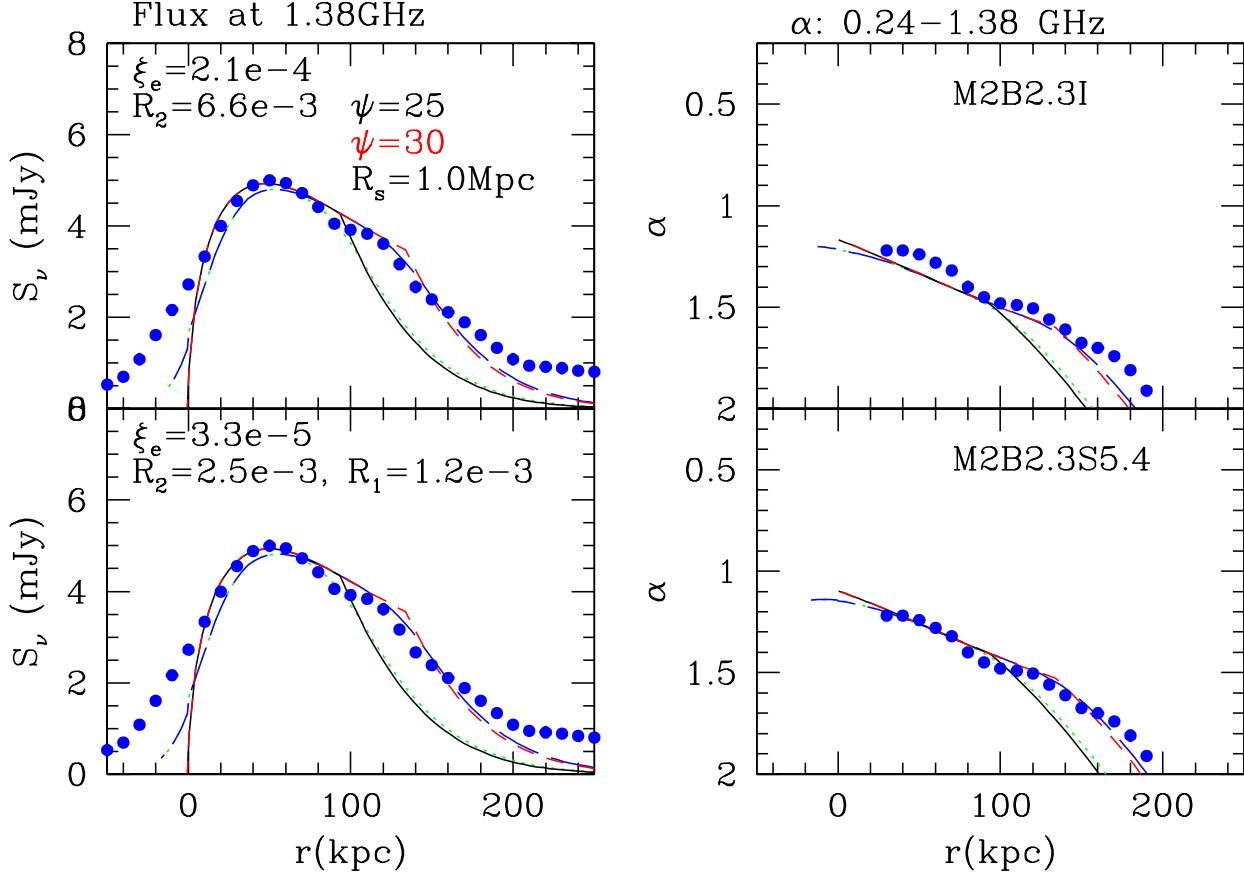


Fig. 4.— The synchrotron flux, S_ν , at 1.38GHz and the spectral index, α , between 0.24 GHz and 1.38 GHz for the M2B2.3I and M2B2.3S5.4 models. Spherical shocks with radius $R_s = 1.0$ Mpc are assumed, and two projection angles, $\psi = 25^\circ$ (solid lines) and 30° (dashed lines), are considered. Dotted and long-dashed lines are the results convolved with a Gaussian beam with the e-width of $12''$. Filled circles are the data points taken from van Weeren et al. (2011) for the radio relic in ZwCl0008.8+5215. The flux is scaled so that the peak has 5 mJy. The required values of the postshock electron CR number fraction, ξ_e , and the ratio of upstream and downstream CR electrons pressure to gas pressure, R_1 and R_2 , are shown.

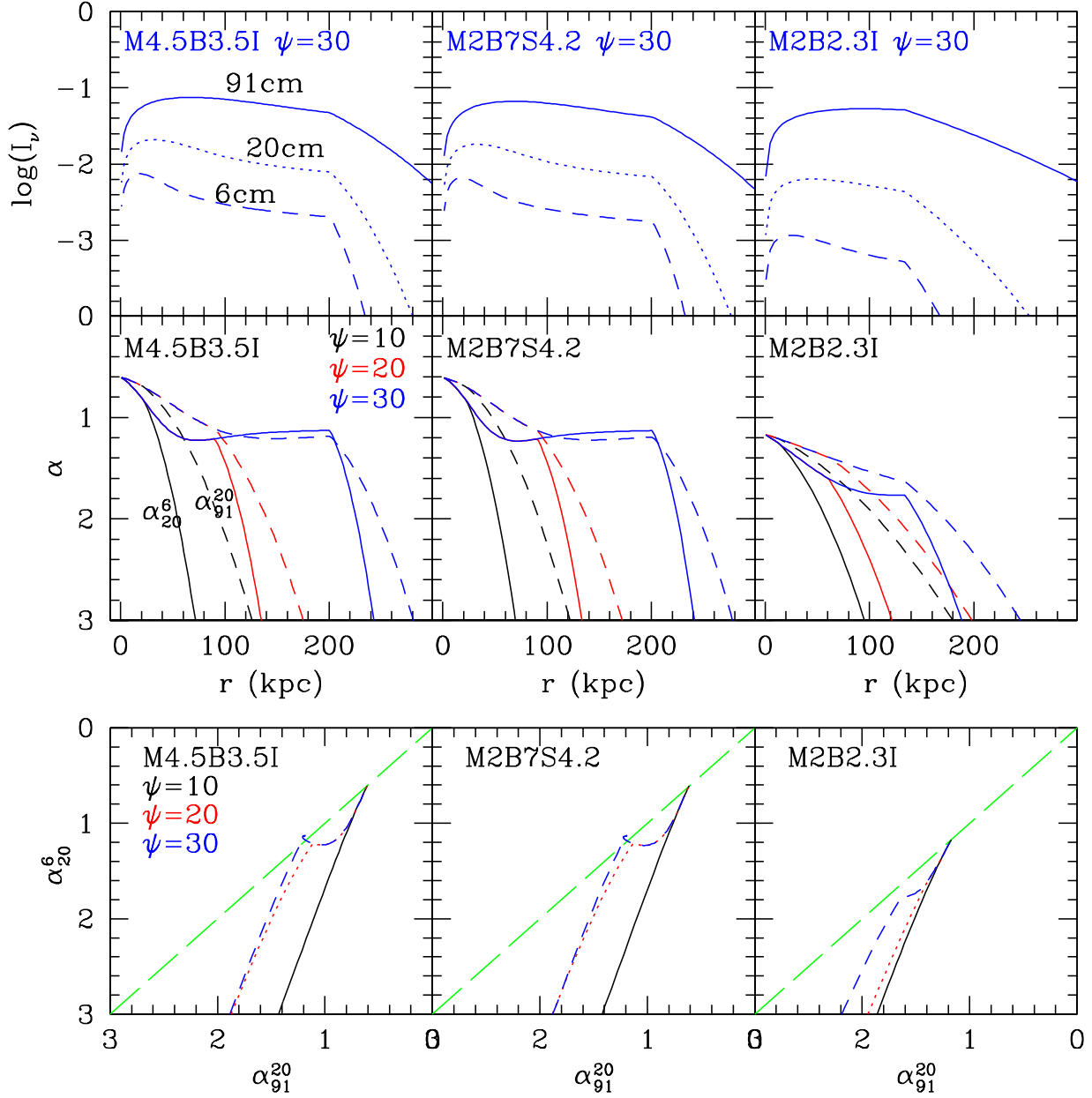


Fig. 5.— Top: The intensities at 6 cm (dashed lines), 20 cm (dotted), and 91 cm (solid) in the case of $\psi = 30^\circ$ for the M4.5B3.5I, M2B7S4.2 and M2B24I models. Middle: The spectral indices α_{20}^6 (solid lines) calculated between 6 cm and 20 cm, and α_{91}^{20} (dashed lines) between 20 cm and 91 cm for three different values of the projection angle, ψ . Bottom: The color-color diagrams of α_{91}^{20} vs α_{20}^6 for three different values of ψ .